International Journal of Heat and Mass Transfer 201 (2023) 123639

Contents lists available at ScienceDirect

International Journal of Heat and Mass Transfer

journal homepage: www.elsevier.com/locate/hmt

L-DED numerical model for sensor embedding

Jon Iñaki Arrizubieta[a,*], Marta Ostolaza[a], Maider Muro[b], Hegoi Andonegi[b], Aitzol Lamikiz[a]

[a] Department of Mechanical Engineering. University of the Basque Country UPV/EHU. Plaza Torres Quevedo 1, 48013 Bilbao, Spain
[b] AZTERLAN, Basque Research and Technology Alliance (BRTA), Durango, Spain

ARTICLE INFO

Article history:
Received 29 June 2022
Revised 28 October 2022
Accepted 5 November 2022
Available online 17 November 2022

Keywords:
L-DED
Model
Thermocouple
Sensor embedding
Adaptive mesh

ABSTRACT

Sensor integration is one of the drivers in modern industry for obtaining real-time data and enabling transition to Industry 4.0. Sensor integration on production systems and tooling is one of the key points for data acquisition. Although several techniques can be applied for sensor integration, Laser Directed Energy Deposition (L-DED) is becoming one of the most relevant, since the sensor can be placed into the manufactured layer-by-layer structure. However, the thermal nature of the L-DED poses a challenge when heat-sensitive parts, such as thermocouples, are to be embedded. In order to ease parametrization and anticipate the behavior of the L-DED process, modeling is an interesting tool that has attracted the attention of academia in the last years. Nevertheless, most models are highly complex and focused on a very local scale or include symmetry assumptions that restrict their use for real applications. In view of this need, in the present research work a thermal model that considers material addition and determines the clad geometry is developed. The model includes an automatic meshing algorithm that adapts the element size by refining the mesh where required. Besides, the model enables 5 axis L-DED, in-process variation of the machine feed rate, and allows to switch on and off the laser to simulate not only the material deposition, but also the idle movements. The model is validated in two steps: single clad deposition on a flat surface and single clads on a 0.3 mm thick thermocouple sheath. Finally, the validated model is used for defining the maximum laser power for embedding virtually a 3 mm diameter K-type thermocouple with a 0.3 mm thick sheath. The results of the simulation are also corroborated by experimental integration of the same thermocouple, which functionality is tested afterwards. Therefore, the L-DED modeling is proven to be an effective tool for manufacturing complex parts on the first try.

1. Introduction

Sensor integration in tooling is one of the key features for data-driven manufacturing, as it enables real-time monitoring of processes such as hot stamping or die casting. However, embedding sensors close to the surface of stamping or die casting tooling, while maintaining the required integrity and material properties, poses a serious challenge. Various approaches have been developed to date in this field.

Alemohammad et al. [1] embedded a fiber optic through a Sn-Pb alloy inside a mold. However, the proposed strategy limits the distance between the sensor and the active surface of the tools, as well as the shape of such surface. For temperature monitoring, Li et al. [2] installed thermocouples in a cutting tool for the development of smart tooling. However, sensors were not embedded inside the cutting tool but placed on its surface. Finally, Jung et al. [3] employed the Selective Laser Melting (SLM) technology to embed a thermocouple in an additively manufactured geometry. The proposed strategy consisted of the manual placement of the sensor in-between the part build-up. The sensor was subsequently covered with a protective layer before continuing with the printing process to achieve the final geometry.

The applicability of the above-described approaches is limited by the manufacturing process employed for the sensor embedding. Therefore, in the present work, the Laser Directed Energy Deposition (L-DED) is proposed based on the higher flexibility and freeform ability that it offers [4]. The L-DED is an Additive Manufacturing process based on the direct injection of the filler material into the melt pool, while a laser beam irradiates on the surface of the substrate and melts both filler and base materials [5]. This process has emerged as one of the alternatives for sensor embedding, as it enables the deposition of material onto the sensor with a minimum dilution. Nevertheless, the set-up of the L-DED process

* Corresponding author at: Department of Mechanical Engineering, University of the Basque Country (UPV/EHU), Plaza Torres Quevedo 1, 48013 Bilbao, Spain.
E-mail address: joninaki.arrizubieta@ehu.eus (J.I. Arrizubieta).

https://doi.org/10.1016/j.ijheatmasstransfer.2022.123639

is still very challenging as the quality of the deposits depends on a high number of parameters and their interaction. Consequently, trial-and-error parametrization methods are the usual go-to procedures for process tuning.

With the aim of saving setup time and reducing the required effort, a relevant number of investigations have been focused on the L-DED process modeling [6]. Nevertheless, the development of a proper model also implies a sequence of high-complexity algorithms and boundary conditions, so different assumptions are introduced to reduce the computational cost [7].

A group of numerical models is aimed at predicting the resulting microstructure of the deposited clad. Akram et al. [8] presented a 2D model, but it requires a predefined melt pool size, and no heat-transfer model is included. Gan et al. [9] calculated the dendrite arm spacing of the resulting microstructure of the deposited material based on the evolution of the temperature in the clad. The same procedure was followed by Tseng and Li [10], but no experimental results for the model validation were provided. Besides, the workload and computation cost of such models are extremely high and assumptions of a symmetrical melt pool and the consideration of only half of the geometry are usual [9,11–13]. Thus, these types of assumptions are only valid for single clad deposition over a flat surface and in case of the laser beam being perpendicular to the substrate. Even 2D models are used to minimize the computational cost [8,14,15], which further reduce the suitability of the model to predict real situations, in which material needs to be deposited on complex-shaped substrates and in any direction.

Another relevant decision when developing a numerical model for L-DED is the consideration or omission of the melt pool dynamics. Their incorporation considerably increases the computational cost and usually, symmetry assumptions are introduced in the model [9,11,12]. Consequently, the applicability of the model is reduced to small domains and limited scenarios as already stated above.

In this direction, Aggarwal et al. [16] studied the effect of the powder particles in the melt pool dynamics when they are introduced into the melt pool. They concluded that under L-DED conditions, the flow pattern in the melt pool is chaotic and random. Consequently, powder particle impingement results in a non-significant Marangoni convection. Similarly, Arrizubieta et al. [17] conducted a research aimed at quantifying the relevance of the melt pool dynamics in the L-DED process modeling. They concluded that for typical L-DED process parameters, the impact of considering the melt pool dynamics is minimal.

Therefore, based on the assumption of a chaotic movement of the molten material, other authors have introduced an enhanced conductivity factor for the molten material, which usually has a value higher than two [18]. For example, Chew et al introduced a factor of 5 for modeling the effective thermal conductivity of the molten AISI 4340 [19]. Similarly, Zhao et al. employed a factor of 5 for an AISI 4140 substrate [12] and Ge et al. used factor of 10 for increasing the thermal conductivity of the 316L when compared to the ambient temperature conductivity [15]. Consequently, despite employing various enhancing factors, in all cases, the effective thermal conductivity within the melt pool is situated between 210 and 225 $W{\cdot}m^{-1}{\cdot}K^{-1}$.

One of the main advantages of neglecting convective heat transfer in the melt pool is the reduction of the computation cost of the model. Therefore, its application can be extended to larger domains and more complex geometries, including multi-track and multilayer simulations. In this field, Guo et al. [20] presented a model for multilayer L-DED. However, it was based on a variance analysis, where the fitting equations were obtained from empirical tests. Also, Joshi et al. [21] developed a multi-track and multilayer model based on finite element analysis that considered the melt pool dynamics. Nonetheless, the momentum due to the impact of the powder particles was neglected, which is the main motion mechanism within the melt pool and no validation evidence was provided. Moreover, Wang et al. [22] developed an analytical model for single clad morphology study under different tilt angles, focused on complex scenarios where 5-axis L-DED is required. Similar to other analytical models, the algorithm was based on experimental tests and consequently, its applicability is limited as compared to numerical approaches, as it is more resource- and time-intensive.

Finally, one of the most attractive advantages of the L-DED is that filler material can differ from the substrate, which enables the enhancement of the properties of the coating. Therefore, multiphase and multimaterial simulations have been developed to consider this scenario. For instance, Ge et al. [15] studied the composition variation when an AISI 316L stainless steel was deposited over an AISI 1045 substrate. The resulting composition of the clad is a combination of both, filler and base, materials. Owing to the random melt pool dynamics [16] almost a constant composition is achieved in each deposited layer, with a real composition proportional to the dilution value. Zhao et al. [12] also developed a multiphase model, where the Marangoni and gravity forces were considered, but the powder particle impinging and buoyancy forces were neglected. Besides, due to the high computational cost, the model only considers half of the clad, which makes the model inappropriate for the simulation of real applications involving multilayer deposition or complex geometries.

Based on the literature review and the lack of practical applications of the models encountered, in the present work a new numerical model is developed to simulate the L-DED process. L-DED models found in the literature typically require unaffordable computational costs, which limit their scalability and application to real industrial problems. For the first time, a model is used to optimize the process parameters for a highly challenging application: direct integration of thermocouples. Therefore, the present work aims at extending the applicability of modeling tools to real and complex engineering problems. In short, the main contribution of the present work is the development of a computationally efficient L-DED model, which enables the process set-up when high precision, but still real-scale geometric and thermal limitations are involved. The validation of the model is performed in two steps: First, the model is validated for single clad deposition on a flat substrate, and then, in a second step, it is validated when depositing material on a thin thermocouple sheath. Finally, in order to show the capabilities of the model, the process parameters for embedding a real thermocouple have been determined based on the model results and a thermocouple has been integrated, both experimentally and numerically.

The model calculates the thermal field of the substrate, defining the limits of the melt pool, and calculates the clad geometry according to the powder distribution at the nozzle outlet and the interaction time. The model includes an adaptive mesh algorithm that refines the mesh in the region close to where the material is being added. Besides, an automatic re-meshing tool is introduced to ensure the quality of the elements and to avoid element distortion during the clad generation.

2. Proposed methodology

The present research aims at developing and validating an L-DED model under real process conditions. In this manner, optimum process parameters that enable the thermocouple embedment without damaging the sensors are determined. The model consists of three mainstays, which are the thermal model (including the material addition algorithm), the machine characteristics (including the laser beam shape and the kinematics), and the material properties. In Section 3 the thermal model is de-

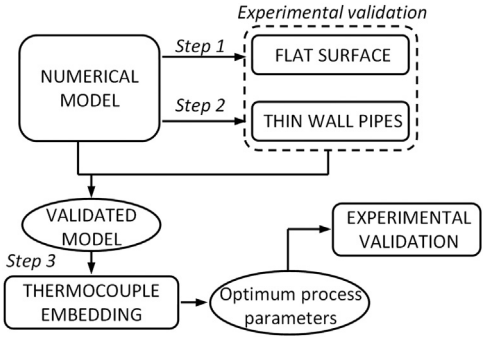

Fig. 1. Methodology followed for the model validation

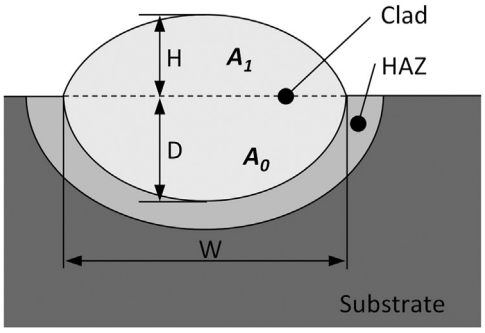

Fig. 2. Clad-geometry characterization, where the height (H), depth (D), and width (W) are highlighted.

tailed, including the meshing algorithm and the material addition. In Section 4 the machine introduced in the model is detailed. Finally, in Section 5 the properties of the employed materials are included. In order to analyze the applicability of the model, the methodology detailed in Fig. 1 has been followed:

First of all, the sensitivity of the model results concerning the element size of the employed mesh is studied (Section 6.1). In addition, in Section 6.2 the influence of the time step in the computational cost is analyzed. Afterwards, the model is validated in two steps. On the one hand, the validity of the model to simulate the L-DED process on a flat tool steel substrate is evaluated for different process parameters (Section 7.1). On the other hand, the model is validated for the deposition of single clads on a thermocouple sheath (Section 7.2).

Once the model is validated for the different substrate configurations and process conditions, it is used to establish the maximum laser power that can be used to embed a thermocouple on a hot stamping tool without causing damage to the sensor. Finally, a thermocouple with a 3 mm tip diameter and a 0.3 mm thickness sheath has been experimentally embedded to test the validity of the model (Section 7.3).

For the model validation, one of the most accepted procedures is the comparison between the longitudinal and transversal sections of the deposited clad [13]. Therefore, in the present research the cross-sections of the clads are evaluated in terms of clad height (H), width (W), and depth (D), see Fig. 2.

In addition, the chemical composition of the clad is assumed to be proportional to the dilution between the filler and base materials. Considering as A_1 the area of the clad above the free surface of the substrate, the dilution is defined as the ratio between the area of the clad situated inside the substrate, A_0, and the total cross-section area of the clad, A_0+A_1 [14]. In the present work the approximation proposed by Abbas and West is used [26], see Eq. (1), which has been used by other authors like Ya et al. [14].

$$d = \frac{A_0}{A_0 + A_1}100\% \approx \frac{D}{D+H}100\% \tag{1}$$

3. Model basis

Hereafter the basis of the model is detailed. The model is entirely developed in Matlab and it solves the heat and material transfer problems in a coupled way. In this manner, the results obtained in each step are the input parameters for the next step. The PDE toolbox is employed for both the mesh generation and the heat transfer equation resolution.

3.1. Modeling approach and assumptions

The assumptions introduced in the model to reduce the computation cost and ease the complexity are detailed hereafter:

1. No molten material movement is considered. Based on the results of previous works [17] this is a valid approximation for typical L-DED parameters.
2. In L-DED, vaporization temperatures are not reached and therefore, material vaporization is ignored [9].
3. The absorptivity of the steel substrate for an Yb:YAG laser is considered to be constant with a value of 0.4 [14]. The same assumption for the absorptivity coefficient is considered by Sihn et al. [23].
4. The laser beam is considered to have a top hat energy distribution.
5. Temperature-dependent properties are considered in the model, including the fusion latent heat of the materials.
6. The composition of the deposited clad is set as constant. Its value is situated between the compositions of the filler and base materials, and it is assumed to be proportional to the clad dilution [15].
7. The energy attenuated by the powder particles is compensated by the heat absorbed by the particles during the inflight and later introduced into the melt pool. Therefore, laser beam attenuation and powder particle heating are neglected.
8. All filler material that is introduced into the melt pool is assumed to adhere to the substrate and become part of it in the successive steps. On the contrary, filler material that falls outside the melt pool is supposed to bounce on the surface of the substrate and is considered lost.

3.2. Thermal model definition

The model solves the heat transfer Eq. (2) in the domain Ω based on the Finite Element Method (FEM), where ρ is the density of the material, c is the specific heat, k is the thermal conductivity of the material, and f is the heat source. Note that the properties of the materials are temperature dependent, but this is not indicated in the equations in pursuit of clarity and facilitate their understanding.

$$\rho c\frac{\partial u}{\partial t} + \nabla \cdot (-k\nabla u) = f \tag{2}$$

Assuming a mesh in the domain Ω and a positive time ($t \geq 0$), the solution of Eq. (2) can be separated into two variables that depend only on the position vector $\{x\}$ and the time t, and are represented by $M_i(x)$ and $G_i(t)$, respectively. According to the FEM formulation this variable separation is defined by Eq. (3):

$$u(\{x\}, t) = \sum_{i=1}^{N} M_i(x)\ G_i(t) \tag{3}$$

In a previous step to apply Greenś formula, the PDE shown in Eq. (2) is multiplied by a function $N_j(x)$ and the result is integrated into the domain Ω, as detailed in Eq. (4):

$$\int_{\Omega}\left[\rho c\frac{\partial M_i G_i}{\partial t}\right]N_j d\Omega + \int_{\Omega}[\nabla \cdot (-k\nabla M_i G_i)]N_j d\Omega = \int_{\Omega} f N_j d\Omega \tag{4}$$

Applying the Greenś formula to Eq. (4), and considering that $\Omega \in R_n$ is a compact set, which boundaries are defined by $\partial\Omega$, and defining as M_i and N_j a pair of functions in Ω that are regular over the entire domain Ω; then, the product rule and divergence theorem give the following expression (5):

$$\int_{\Omega} \rho c M_i N_j \frac{\partial G_i}{\partial t} d\Omega + \int_{\Omega} \left[k \nabla M_i \cdot \nabla N_j\right] d\Omega G_i + \int_{\partial\Omega} \left[(-k \nabla M_i) \cdot n N_j\right] d\Gamma G_i = \int_{\Omega} f N_j d\Omega \tag{5}$$

Now, the boundary conditions (BC) can be imposed, where n represents the normal direction to the boundary in which the BC is being defined.

$$\int_{\Omega} \rho c M_i N_j \frac{\partial G_i}{\partial t} d\Omega + \int_{\Omega} \left[k \nabla M_i \cdot \nabla N_j\right] d\Omega G_i + \int_{\partial\Omega} \left[\left(-k \frac{\partial M_i}{\partial n}\right) N_j\right] d\Gamma G_i = \int_{\Omega} f N_j d\Omega \tag{6}$$

The PDE equation above can be expressed in matrix notation as detailed in Eq. (7), which is solved over the time to obtain the temperature $u(\{x\}, t)$ in each node of the mesh situated in the position $\{x\}$ at the time step t. As in the present case the coefficients are temperature dependent, the model is non-linear, the matrices in Eq. (7) are reevaluated and refactorized in each time step.

$$M \frac{\partial G}{\partial t} + KG = F \tag{7}$$

3.3. Trajectory generation

The L-DED head position is defined by the matrix $[LP(t)]$, which consists of 7 columns: the first three correspond to the XYZ coordinates, whereas the 4th and 5th columns correspond to the A and B rotation axes, around the X and Y axes, respectively. Lastly, the 6th and 7th columns correspond to the laser power and machine feed rate, respectively. This enables feeding the model with commands similar to the CNC programs employed in industrial L-DED machines. The laser is automatically switched on when a power value is introduced in the 6th column and switched off when a zero-laser power is introduced. This permits the simulation of multi-clad depositions, with the corresponding cooling stage between the deposition of successive clads.

$$[LP(t)] = \begin{bmatrix} \{LP(1,t)\} \\ \{LP(2,t)\} \\ \{LP(3,t)\} \\ \{LP(4,t)\} \\ \{LP(5,t)\} \\ \{LP(6,t)\} \\ \{LP(7,t)\} \end{bmatrix}^T \tag{8}$$

The model automatically discretizes the introduced trajectory in multiple steps according to the space discretization determined by the user. In the present case, an *r/4=0.15 mm* spatial discretization is used in all simulations, being r the laser beam radius.

3.4. Initial conditions

The initial conditions are required to launch the simulation. In Eq. (9) the parameter $u(\{x\}, 0)$ stands for the temperature at any $\{x\} = (x, y, z)$ position inside the domain Ω at the time instant $t=0$, and $u_0(\{x\})$ is the initial temperature, which can be defined as a constant value or a function.

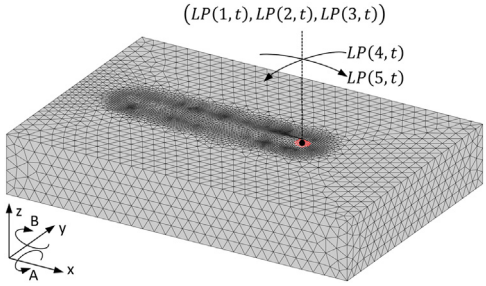

Fig. 3. Adaptive mesh where the region Γ_1 is highlighted in red and the position of the laser is defined at the time instant t.

$$u(\{x\}, 0) = u_0(\{x\}) \tag{9}$$

In the present case, a constant 25°C room temperature is considered as the initial temperature in all simulations.

3.5. Boundary conditions

Three types of boundary regions are defined in the model: Γ_1 is the region where the laser beam irradiates the free surface of the workpiece, $\Gamma_2$is the lower face in contact with the support system, and Γ_3 comprises the rest of the faces in contact with the atmosphere.

The laser beam is defined as a top-hat heat source. Thus, the energy is distributed homogeneously in the surface region situated inside the laser beam, whose radius is r, see Fig. 3. The parameter α in Eq. (10) stands for the laser beam absorptivity of the substrate. Steen and Mazumder [24] reported that for a 1.07 µm wavelength laser radiation, steel substrates present an absorptivity around 40% both at room and high temperatures. The same 0.4 constant absorptivity value was also measured by Chew et al. [19] for steels and also, a constant 0.4 absorptivity value was employed by Ya et al. [14] for AISI 420 and AISI 4140 steels. Therefore, in the present research, a constant $\alpha = 0.4$ absorptivity value is employed.

$$f(\{x\}, t) = \frac{\alpha \; LP(6,t)}{\pi r^2} \; if \; (\{x\}, t) \in \Gamma_1 \tag{10}$$

Besides, the model considers the effect of the divergence angle of the laser beam, θ, as the free surface of the workpiece differs from the focal plane of the laser. The absolute value of the laser defocus, named as δ, modifies the radius of the laser beam, r, according to the following Eq. (11). The divergence angle, θ, is obtained from the shape of the laser beam at the L-DED head exit, which is defined by the machine parameters in Table 1.

$$r = \frac{w_0}{2} + |\delta| \tan\theta \tag{11}$$

The laser defocus, δ, needs to be evaluated in every step of the laser position $\{LP\}$ and it is defined as the value that minimizes

Table 1
Machine parameters employed in the simulations.

Machine characteristic	Value
Laser beam diameter, w_0	1.2 mm
Beam Parameter Product, *BPP*	4 mm·mrad
Fiber core diameter, d_c	100 µm
Fiber ring diameter, d_r	400 µm
Focal length, L	200 mm
Powder initial temperature, u_p	60°C
Powder spot radius, R	1.5 mm

the residue of the following Eq. (12). Note that the sum goes from 1 to 3, as each node has three degrees of freedom:

$$\left(\sum_{i=1}^{3}\left[(\{x_i\},t)-\delta\begin{Bmatrix} sin(\{LP(5,t)\}) \\ sin(\{LP(4,t)\}) \\ cos(\{LP(4,t)\})cos(\{LP(5,t)\}) \end{Bmatrix}^T \{LP(\{i\},t)\}\right]^2\right)^{1/2} = 0 \tag{12}$$

Regarding the second boundary condition, Γ_2, the simulated part is considered as simply supported at the lower face. The bigger size of the support system when compared to the workpiece and the good surface finish of both faces ensures heat conduction via conductivity. Consequently, the lower face is modeled as a heat sink, with a constant temperature and equal to the room temperature u_∞.

$$u(\{x\},t) = u_\infty \; if \; (\{x\},t) \in \Gamma_2 \tag{13}$$

In all faces that are not in contact with the supporting system convective and radiation heat losses are considered according to Eq. (14): h_c is the convective coefficient, ε is the radiative emittance, σ is the Stefan-Boltzmann constant ($5.67{\cdot}10^8$ $W{\cdot}m^{-2}{\cdot}K^{-4}$) and room temperature is defined by u_∞.

$$f(\{x\},t) = -h_c(u(\{x\},t)-u_\infty) - \varepsilon\sigma\left(u(\{x\},t)^4 - u_\infty^4\right) \; if \; (\{x\},t) \in \Gamma_3 \tag{14}$$

3.6. Material addition

For the material addition, two strategies can be differentiated [7]: the element birth-death and the adaptive mesh. In the first option, a structured mesh is used, and the elements are activated as material is being deposited and they get filled. This action is named as element birth [25]. The main problems of this first alternative are that, before running the simulation, the geometry of the deposited clad needs to be known and that a higher number of elements that are employed systematically. On the contrary, in the adaptive mesh algorithm, the mesh is being distorted as the filler material is injected into the melt pool, which provides a more cost-effective material addition algorithm.

In the present work, the material deposition is modeled as an adaptive mesh algorithm based on the nodal displacement. According to assumptions introduced in Section 3.1, all filler material that falls inside the melt pool is considered to adhere to the substrate and become part of it for future steps. On the contrary, filler material that falls outside the melt pool is supposed to bounce off and is considered lost. Therefore, the model only considers the filler material that falls inside the melt pool. In other words, the material is added in all surface nodes that exceed the melting temperature T_{fus}. The vectorial distance displaced by each node and the condition that the nodes need to fulfill are represented in Eq. (15).

$$d\{\{x\},t\} = \begin{Bmatrix} d(\{x(1)\},t) \\ d(\{x(2)\},t) \\ d(\{x(3)\},t) \end{Bmatrix}^T \; where: (\{x\},t) \in \Gamma \wedge \; u(\{x\},t) > T_{fus} \tag{15}$$

In powder-based L-DED the filler material flow approximates to a Gaussian distribution at the focal plane, with a maximum concentration at the axis center. Thus, the distance displaced for each node is specified in Eq. (16), where $\dot{m}$ is the filler material mass rate, ρ_p is the density of the filler material at the temperature u_p at which powder particles are introduced into the melt pool, R is the radius of the powder flow at the focal plane, and dp is the distance between the laser position *{LP}* and the node in which displacement is being calculated.

$$\begin{aligned} d(\{x(1)\},t) &= \frac{2\dot{m}dt}{\rho_p(u_p)\pi R^2} e^{-2\left(\frac{\{dp(\{2\},t)\}^2+\{dp(\{3\},t)\}^2}{R^2}\right)} sin(\{LP(5,t)\}) \\ d(\{x(2)\},t) &= \frac{2\dot{m}dt}{\rho_p(u_p)\pi R^2} e^{-2\left(\frac{\{dp(\{1\},t)\}^2+\{dp(\{3\},t)\}^2}{R^2}\right)} sin(\{LP(4,t)\}) \\ d(\{x(3)\},t) &= \frac{2\dot{m}dt}{\rho_p(u_p)\pi R^2} e^{-2\left(\frac{\{dp(\{1\},t)\}^2+\{dp(\{2\},t)\}^2}{R^2}\right)} cos(\{LP(4,t)\})cos(\{LP(5,t)\}) \end{aligned} \tag{16}$$

The distance between the L-DED head position and the mesh nodes is defined by the following Eq. (17), where dp is a matrix in which each column provides the distance between that node number position and the DED head:

$$\{dp(\{x\},t)\} = \{(\{x\},t) - \{LP(\{1:3\},t)\}\}^T \tag{17}$$

Gan et al. [9] and Arrizubieta et al. [17] considered the interaction between the injected powder and the laser beam during the inflight trajectory of the powder particles. In their models, the energy absorbed by the powder particles is later introduced into the melt pool when the particles are inserted. According to Ya et al. [14], the total energy introduced into the system in each step is calculated through Eq. (18), where P is the laser power, P_{at} is the attenuated power by the powder particles, and α_s and α_p are the absorptivity of the substrate and the powder, respectively.

$$Q_{total} = (\alpha_s(P-P_{at}) + \alpha_p P_{at})dt \tag{18}$$

Assuming that the absorptivity of the substrate and the powder are similar, $\alpha_s \approx \alpha_p$, the heat lost by the attenuation is compensated by the thermal energy gained by the powder particles before they reach the melt pool. Therefore, Eq. (18) is simplified and the influence of the powder attenuation is eliminated. Consequently, the total energy introduced by the laser beam into the substrate depends only on the absorptivity and the interaction time. This statement is the basis for the 7th assumption indicated in Section 3.1.

When the filler material is introduced into an element and this increases its volume, both material and energy conservation need to be considered. The temperature of the displaced nodes needs to be adapted to compensate for the fraction of powder introduced into each element. The variation of the temperature of the displaced node is defined proportional to the increase of the element volume, where e and u_p stand for the element edge size and the temperature of the particles when they reach the melt pool respectively.

$$u(\{x\},t) = \frac{e\,u(\{x\},t) + |d\{\{x\},t\}|u_p}{e + |d\{\{x\},t\}|} \; where: (\{x\},t) \in \Gamma \wedge \; u(\{x\},t) > T_{fus} \tag{19}$$

3.7. Mesh generation

The employed mesh consists of tetrahedral elements, whose size adapts to the contours of the studied volume Ω. First-order elements are used to avoid numerical instabilities that could arise because of the high-temperature gradients produced in L-DED.

The developed meshing algorithm is based on the meshing command from the PDE toolbox of Matlab. However, it reduces the element size automatically in each step in the regions where high temperature gradients are expected and it adapts the mesh to the geometry of the deposited material. In Fig. 3, an example of the mesh is given for a single clad deposition on a flat surface.

At the end of each time step, the surface nodes where the L-DED process adds material are displaced the distance $d(\{x\},t)$ defined in Eq. (16). Therefore, the new control volume is defined as:

$$\Omega(\{x\},t+dt) = \Omega(\{x\},t) + d\{\{x\},t\} \tag{20}$$

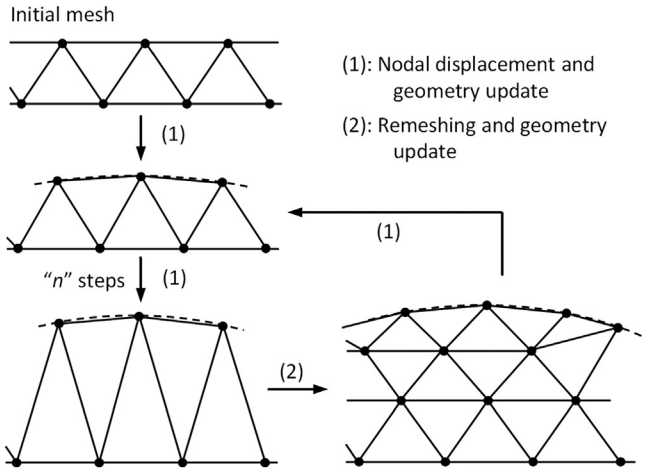

Fig. 4. Automatic remeshing to avoid mesh degeneration when material is added.

Successive node displacements increase the skewness of the elements and can adversely affect the convergence and accuracy of the results. Therefore, every n iterations, an automatic remeshing operation is performed, see Fig. 4. The new geometry in each time step $(t + dt)$ is defined by the surrounding geometry, Γ, of the mesh at the end of the previous time step, whereas the geometry is filled with a new mesh that ensures the quality of the elements.

$$\Omega(t + dt) = fill[\Gamma(\{x\}, t + dt)] \tag{21}$$

The temperature field inside the new control volume Ω defined by the new nodes position $\{y\}$ is calculated by means of linear interpolation of the nodal temperatures of the old mesh that is being substituted.

$$u(\{y\}, t + dt) = interp[u(\{x\}, t + dt)] \tag{22}$$

The activation of the remeshing increases the computational time considerably because a new mesh needs to be generated, but it is necessary to ensure the quality of the mesh. Therefore, in the present case, the remeshing algorithm is activated every 3-10 steps, depending on the process parameters and the amount of material introduced per unit length of the clad.

4. Experimental setup

The experimental tests for the model validation are performed on a Trucell 3000 laser center, which is equipped with a 3 kW solid-state laser. The laser works in CW mode at a 1.03 µm wavelength and it is focused on a 1.2 mm spot diameter. The laser comprises two fibers for the beam transmission, namely, core and ring configurations. In the present work, the core fiber with a top-hat energy distribution at the focal plane is used in all tests. Argon gas is used to generate the protective atmosphere at a 12 $l{\cdot}min^{-1}$ flow and helium is employed as the drag gas at a 4 $l{\cdot}min^{-1}$ rate.

The filler material selected for all tests is the AISI H13 tool steel powder, which is supplied by FST with a 45-125 microns diameter range and fabricated via gas atomization to ensure a spherical shape of the particles. This decision is driven by the final application of the work, which is the integration of thermocouples into hot stamping tools. A coaxial nozzle is employed for injecting the powder into the melt pool. The powder concentration at the focal plane follows a Gaussian distribution with a 2.99 mm diameter, according to the manufacturer. In Table 1 the specifications employed to define the digital twin of the machine are shown.

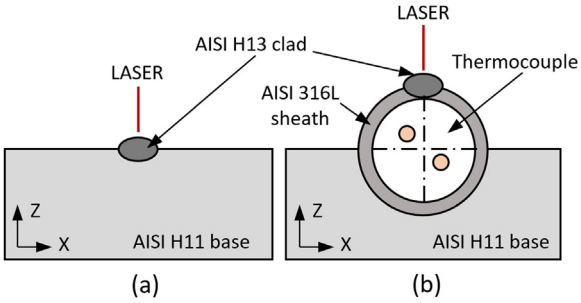

Fig. 5. Scheme of the tests and the employed materials.

For the cross-section analysis, the samples are cut using a metallographic saw. Afterwards, they are mounted, ground, and polished, following an appropriate metallographic procedure. Lastly, they are etched with Nital4. In this manner, the microstructure is revealed, and the differentiation of the clad from the non-melted substrate is facilitated. A Leica DCM 3D confocal microscope is employed for inspection purposes and to define the dimensions of the deposited clad. Three sections of each test are analyzed and their average is used for validation purposes.

5. Employed materials

In the flat surface tests, both filler and base materials are tool steels. Filler material is the AISI H13 tool steel, whereas the base material is the AISI H11 tool steel. When depositing material in the thin wall tubes, see Fig. 5, the filler and base materials are maintained. However, the deposits are made onto an AISI 316L stainless steel sheath, which is similar both in terms of material and dimensions to the enclosure of the thermocouples. The used thermocouples are K-type, with an AISI 316L stainless steel sheath and mineral insulated. Thermocouples have a 3 mm external diameter and are custom build by TC Direct.

The chemical composition of the employed materials is detailed in Table 2. For the AISI H11 and H13 the average values provided by the ASTM A681 standard are considered, as for the AISI 316L stainless steel the composition provided by the thermocouple manufacturer is employed.

The thermophysical properties of the materials involved in the model are calculated through the ThermoCalc software. This software is based on the CALPHAD methodology. Thus, for each material system, the state (phase equilibrium and phase compositions) that minimizes the Gibbs free energy is determined. Accordingly, the thermodynamic properties of the material system are calculated. In this manner, the solidus, liquidus, and fusion temperature of AISI H13, AISI H11 and AISI 316L are determined (Table 3).

Table 2
Chemical composition of the employed materials (wt%).

ASTM A681	C	Mn	P	S	Si	Cr	Ni	V	Mo	Fe
AISI H13	0.385	0.4	0.03	0.03	1.025	5.125	-	1	1.425	Bal.
AISI H11	0.4	0.4	0.03	0.03	1.025	5.125	-	0.45	1.35	Bal.
AISI 316L	0.015	1	0.04	0.03	0.375	18	13	-	2.75	Bal.

Table 3
Fusion temperatures for the employed material. Liquidus and Solidus temperatures predicted by the ThermoCalc software and the fusion temperature of each material employed in the model.

Temperature [°C]	AISI H13	AISI H11	AISI 316L
T_{sol}	1377	1400	1400
T_{liq}	1478	1478	1439
T_{fus}	1428	1439	1420

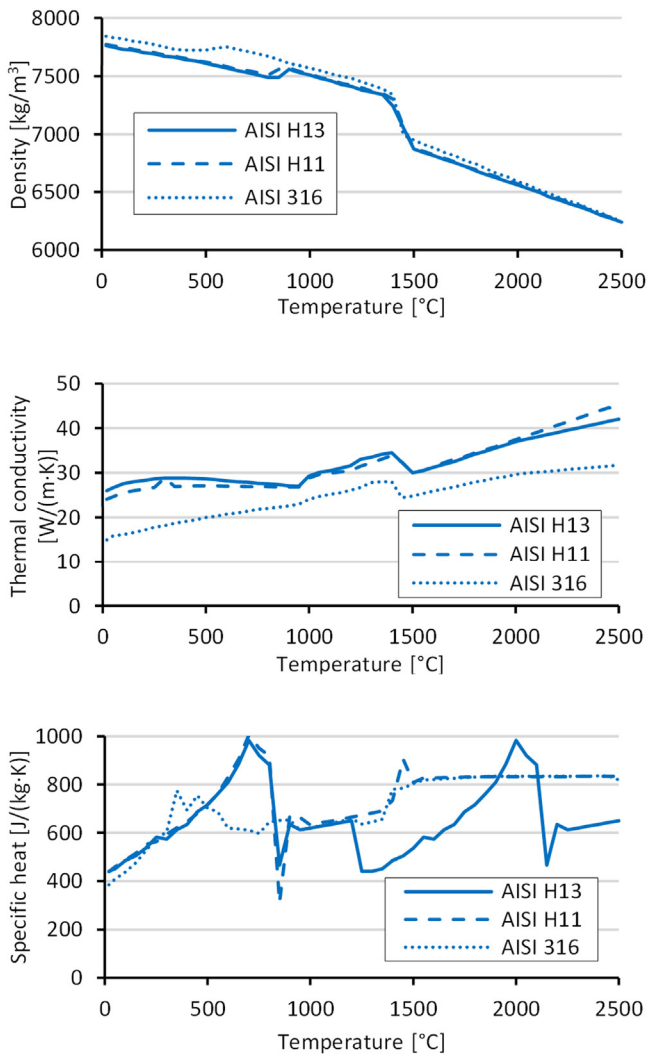

Fig. 6. Density, thermal conductivity, and specific heat characterization of the AISI H13, AISI H11 and AISI 316 steels.

In addition, the temperature-dependent thermophysical material properties of the alloys in the desired range (25 – 2500°C) are calculated, i.e., the density, the thermal conductivity, and the specific heat (Fig. 6). These properties are fed to the model to facilitate the resolution of the thermal field throughout the simulation. For the calculation of the equilibrium phase diagram in the temperature range of 20 to 2500°C, the database TCFE9: Steels/Fe-Alloys v9.3 and MOBFe4: Steels/Fe-Alloys Mobility v4.0 is used.

The dilution of the clad into the base material plays a relevant role in the resulting composition of the clad. In order to solve this issue, the properties of the clad in all tests are calculated based on the dilution between the clad material and the base material. Consequently, a 0% dilution implies that the properties of the clad are those of the filler material, AISI H13 in the present case. On the contrary, a 100% dilution implies that no clad is being deposited and the properties of the generated track are those of the base material, AISI H13 or AISI 316 depending on the test.

6. Model calibration

6.1. Element-size sensitivity

In order to ensure the validity of the results provided by the developed numerical model, the invariability of the results with regard to the mesh needs to be proven. The region close to the clad is the region that requires the higher mesh resolution due to the higher thermal gradients. Thus, the first step is to define an element size in that region, where the obtained results are accurate and independent of the employed mesh.

Too small elements imply excessive computational cost, but too large elements can introduce considerable numerical error in the model. Reference L-DED parameters are considered for the element size sensitivity analysis: 600 W power, 450 mm·min^{-1} feed rate, and 3.5 g·min^{-1} powder mass flow. Starting from a 0.3 mm element size, the element size is progressively reduced until a 0.05 mm value. In each case, the height and width of the simulated clad are compared. Both filler and base material are AISI H13 for the model calibration and a 40 × 20 × 5 mm^3 substrate is considered. In all tests, a 0.02 s constant time step is employed for discretizing the laser path.

As it can be seen in Fig. 7, for an element size below 0.2 mm the height and width of the clad remain constant. Therefore, a 0.2 mm element size is established as adequate in the region close to the melt pool and the generated clad. This minimum element size in the high resolution region and a maximum of 2 mm in the region far from the clad, generates a mesh of approximately 10,000 elements. It takes about 16 minutes to simulate a 10 mm long clad on a PC with 8 Gb RAM and an Intel i7 processor.

6.2. Time step increase

The influence of the time step is also analyzed before running the simulations. If smaller time steps are employed, more steps are required for simulating the same clad length. Nevertheless, small time steps imply that the thermal field between two successive steps does not vary significantly and the time per iteration is reduced. On the contrary, a higher time step reduces the number of steps, but increases the solving time of each step. The only calculation that does not depend on the time step is the clad geometry determination, which only depends on the mesh size. The calculation of the clad geometry takes between 5 and 10 seconds per iteration. In Fig. 8 a detailed analysis of the calculation times for a straight 10 mm long clad are shown. The same parameters as in Section 6.1 are employed and a constant minimum element size of 0.2 mm is used.

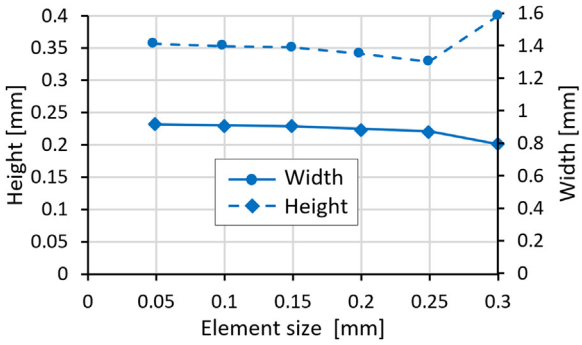

Fig. 7. Element size sensitivity results. Process conditions: 600 W laser power, 450 mm·min^{-1} feed rate, and 3.5 g·min^{-1} powder mass flow.

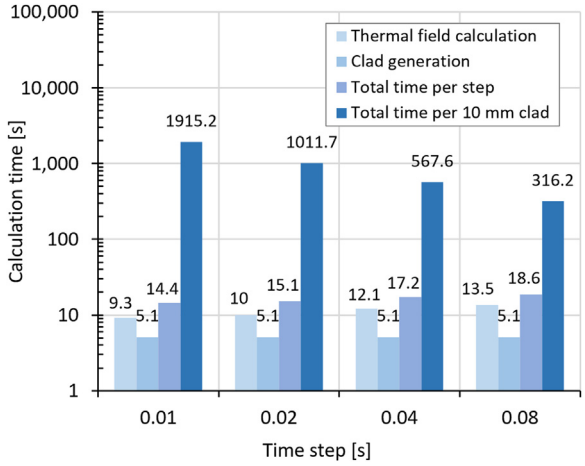

Fig. 8. Computational time analysis for different time steps.

A 0.02 s time step is selected for the present study, which has a relatively high calculation time, but also results in a smoother clad than higher time steps. For a 450 mm·min^{-1} feed rate and a 1.2 mm laser spot, a 0.02 s time step implies that the laser moves 0.15 mm in every step; that is, a quarter of the laser radius.

Also, it is noticed that the calculation time varies slightly with the process parameters. Higher laser powers generate more pronounced temperature gradients and it takes more time to obtain the results. For instance, in the simple clad deposition on tube (Section 7.2): 1896 s, 1964 s, and 2006 s calculation times are required for the 150 W, 200 W and 250 W tests, respectively.

7. Results and discussion

As detailed in the methodology section, the model is validated in two steps. Afterwards, in a third step, the model is used for determining the required laser power for embedding a thermocouple into a hot stamping tool. Therefore, the results are presented accordingly.

7.1. Simple clad deposition on flat surface

In Table 4 the designed DOE for the model validation when depositing AISI H13 tool steel powder on a flat AISI H11 tool steel surface is detailed. The central parameters are a 600 W laser power

Table 4
DOE test parameters.

Test	P [W]	F [mm·min^{-1}]	M [g·min^{-1}]
1	600	450	2.09
2	500	300	2.5
3	700	300	2.5
4	700	600	2.5
5	500	600	2.5
6	600	237.87	3.5
7	600	450	3.5
8	741.42	450	3.5
9	458.58	450	3.5
10	600	450	3.5
11	600	450	3.5
12	600	450	3.5
13	600	662.13	3.5
14	700	300	4.5
15	500	300	4.5
16	500	600	4.5
17	700	600	4.5
18	600	450	4.91

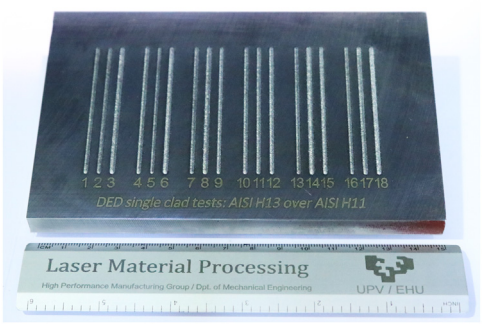

Fig. 9. Final aspect of the deposited 18 clads of AISI H13 over an AISI H11 substrate.

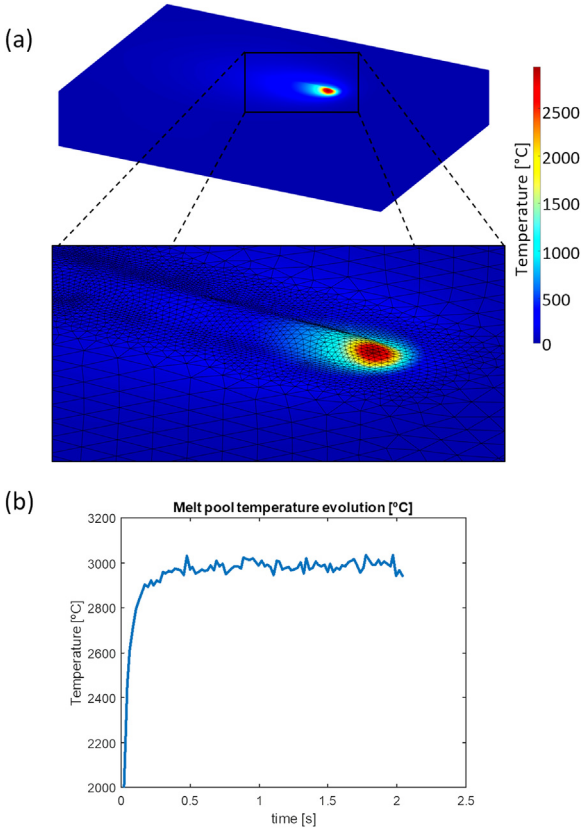

Fig. 10. a) Thermal field and a detail of the mesh at the t=2 s time instant in Test 10 and b) the evolution of the maximum melt pool temperature.

(P), a 450 mm·min^{-1} feed rate (F), and a 3.5 g·min^{-1} powder mass flow (M). A total number of 18 runs are performed using a Central Composite Design, with an orthogonal quadratic configuration and 4 repetitions for the center point. In Fig. 9 the deposited simple clads are shown.

A 40 × 20 × 5 mm^3 volume is modeled and a 30 mm long clad between points (5, 10, 5) and (35, 10, 5) is simulated in every test. Before each experimental test, the part is cooled down until room temperature is reached. Therefore, in all simulations, a 25°C initial temperature is stablished. The lower face, which is in contact with the machine table, is considered to be at a 25°C constant temperature. In the remaining faces, which are in contact with the atmosphere, a 20 W·m^{-2}·K^{-1} convection coefficient is introduced.

In the model, the maximum temperatures of the melt pool are monitored, and the evolution of the thermal field is calculated as the clad is being deposited. In Fig. 10(a) the thermal field during the deposition of the clad in Test 10 is illustrated. Also, the clad

Table 5
Results of the experimental tests and model for the simple clad deposition of flat surface.

Test	H [mm]			W [mm]			D [mm]			Dilution (%)		
	Exp.	Model	error [%]	Exp.	Model	error [%]	Exp.	Model	error [%]	Exp.	Model	error [%]
1	0.14	0.14	3.44	1.37	1.28	7.08	0.53	0.49	7.38	78.95	78.32	0.80
2	0.25	0.24	5.06	1.35	1.30	3.89	0.44	0.42	4.54	64.03	64.15	0.18
3	0.31	0.31	1.12	1.67	1.61	3.79	0.57	0.58	1.21	64.87	64.89	0.03
4	0.16	0.14	8.46	1.37	1.43	3.86	0.54	0.53	1.00	77.66	78.87	1.54
5	0.10	0.12	13.84	1.09	1.14	4.45	0.43	0.39	9.40	80.69	76.70	5.21
6	0.47	0.52	8.31	1.55	1.48	5.03	0.50	0.46	7.67	51.18	47.16	8.51
7	0.26	0.25	5.40	1.35	1.34	0.68	0.45	0.46	1.74	63.42	65.03	2.48
8	0.28	0.27	3.33	1.64	1.50	9.65	0.49	0.54	9.78	63.67	66.74	4.61
9	0.20	0.22	8.33	1.12	1.06	6.53	0.36	0.34	6.70	64.00	60.43	5.90
10	0.26	0.25	7.03	1.35	1.34	0.63	0.47	0.46	2.30	63.99	65.03	1.59
11	0.25	0.25	2.00	1.32	1.34	1.26	0.46	0.46	0.67	64.73	65.03	0.46
12	0.25	0.25	2.32	1.39	1.34	3.92	0.45	0.46	2.21	63.99	65.03	1.59
13	0.18	0.16	9.64	1.27	1.20	5.53	0.46	0.42	9.48	72.28	72.31	0.04
14	0.62	0.53	17.17	1.71	1.48	15.88	0.42	0.44	4.82	40.48	45.57	11.17
15	0.42	0.43	2.43	1.38	1.31	5.00	0.30	0.33	7.13	42.18	43.39	2.79
16	0.22	0.22	3.02	1.12	1.10	2.26	0.32	0.34	3.90	59.12	60.79	2.75
17	0.28	0.24	16.00	1.53	1.34	14.20	0.40	0.47	15.41	58.74	66.13	11.17
18	0.36	0.34	5.87	1.47	1.42	3.35	0.38	0.42	9.91	51.18	55.19	7.27

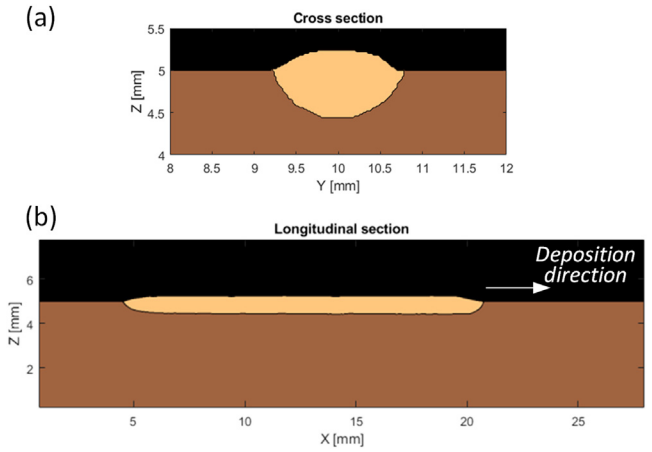

Fig. 11. a) Transversal and b) longitudinal cross sections of the clad deposited in Test 10.

area is magnified and the temperature field and the mesh are represented in order to show the adaptability of the latter to the clad geometry.

The model also determines the historically melted nodes, which enables the determination of the geometry of the clad in the longitudinal and transversal section. In Fig. 11 the transversal and longitudinal cross sections of the clad deposited in Test 10 are shown. The light brown represents the material melted by the laser, whereas the dark brown is the base material, AISI H11, not melted by the laser during the L-DED process.

Once all tests have been simulated, in Table 5 the experimental results (Exp.) are compared with the numerical model. Besides, the values of the dilution are calculated based on Eq. (1). As it can be seen, the error in the clad height (H), width (W), depth (D), and dilution is below 10 %, but there are a few exceptions. On the one hand, Test 5 presents an error higher than 10% in the clad height, but the variation corresponds to 0.017 mm, therefore, the deviation is considered low. On the other hand, Tests 14 and 17 present errors higher than 10% in the three analyzed dimensions. The model overpredicts the clad height and width, but underestimates the depth. These tests correspond to the maximum laser power and powder mass rate employed, 700 W and 4.5 g·min^{-1}, respectively. Therefore, it is concluded that the model loses accuracy for parameter combinations with higher laser powers and powder mass rates.

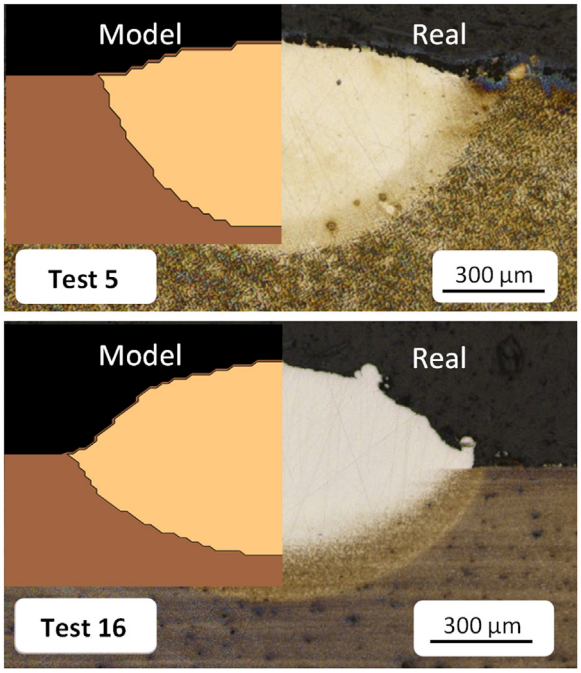

Fig. 12. Comparison between the simulated and the experimental cross section of the clads in Test 5 and 16.

As an example, in Fig. 12 the cross sections obtained experimentally and numerically in Tests 5 and 16 are overlapped. The procedure detailed in Section 4 is used for the metallographic preparation, and the polished cross sections are etched with Nital4 to reveal the geometry of the clad and the molten area. Similarly, the molten region is represented in orange in the model results. As it can be seen, a high resemblance between the numerical and experimental results is obtained. Hence, it is concluded that the numerical model can predict the clad geometry with high accuracy.

7.2. Simple clad deposition on tube

Once the model is validated for L-DED on a flat surface, the second step is to study the scenario in which single clads are deposited on cylindrical tubes. For this purpose, a thermocouple with an AISI 316 sheath of 3 mm external diameter and 0.3 mm thickness is employed. In order to avoid perforating the sheath, lower

Table 6
Test parameters for simple clad deposition on tube.

Test	P [W]	F [mm·min^{-1}]	M [g·min^{-1}]
20	150	450	3.24
21	200	450	3.24
22	250	450	3.24

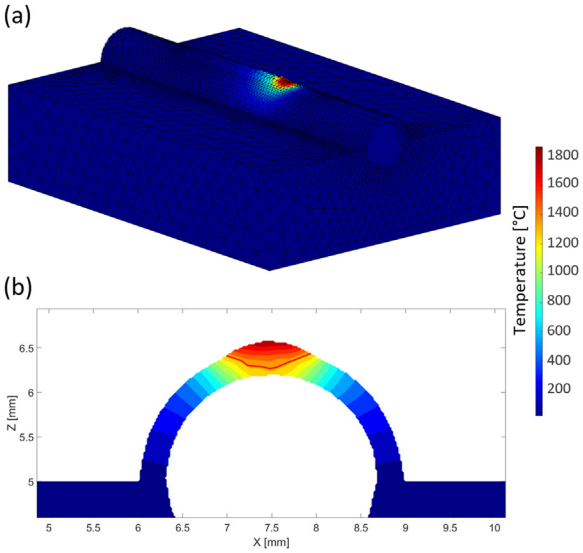

Fig. 13. a) Thermal field during plotted over the mesh in Test 21 and b). Detail of the section of the deposited clad onto the thermocouple in the laser centerline.

laser powers are employed. The tests in Table 6 are numbered from 20 onwards to avoid using the same test numbers as in the previous section.

The thermocouple is inserted on an AISI H11 base, which has a 3 mm diameter cylindrical groove to longitudinally hold its lower half. The AISI H11 base has a 30 × 15 × 5 mm^3 volume and a 20 mm long clad is simulated on the top of the cylindrical thermocouple between points (5, 7.5, 6.5) and (25, 7.5, 6.5). In Fig. 13 the thermal field during Test 21 at the position corresponding to coordinates (17, 7.5, 6.5) is shown. A new thermocouple is used in each experimental test. Therefore, in all simulations, a 25°C initial temperature is set. The lower face, which is in contact with the machine table, is at a 25°C constant temperature. In the remaining faces in contact with the atmosphere a 20 W·(m·K)$^{-1}$ convection coefficient is considered. The interior of the thermocouple is mineral insulated and therefore, it is considered adiabatic. This assumption permits neglecting the interior geometry of the tube. Hence, the size of the mesh is reduced and so is the resulting computational cost.

In Fig. 14 the evolution of the maximum temperatures for tests 20-22 is shown. Higher laser powers result in higher temperatures, but all three processes are stable once a steady regime is reached after 0.2 seconds. The red line in the cross sections represents the boundaries of the melt pool. As it can be seen, in Test 22 the laser pierces the wall of the thermocouple. Therefore, the 250 W laser power is concluded to be too high for depositing on a 0.3 mm thick sheath.

Good accordance between the model and experimental results is obtained, Fig. 15, and as is shown in Table 7, an error below 10% is obtained in all cases. Same magnitude errors as those obtained in Section 7.1 are attained. Test 22 pierces the sheath of the thermocouple. Therefore, the depth of both the experiment and model is given as 0.3 mm and no value of the error is provided, as it makes no sense.

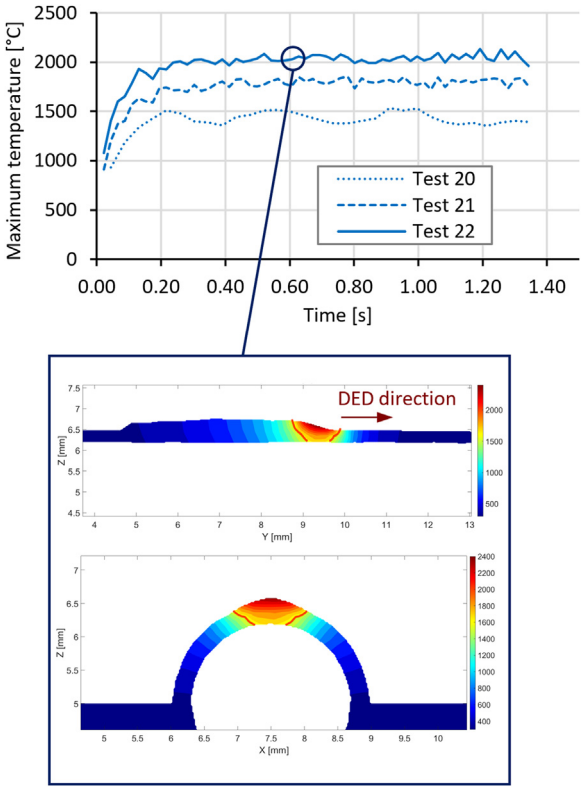

Fig. 14. Maximum temperature evolution and cross sections of the L-DED process of test 22. The red line represents the boundaries of the melt pool.

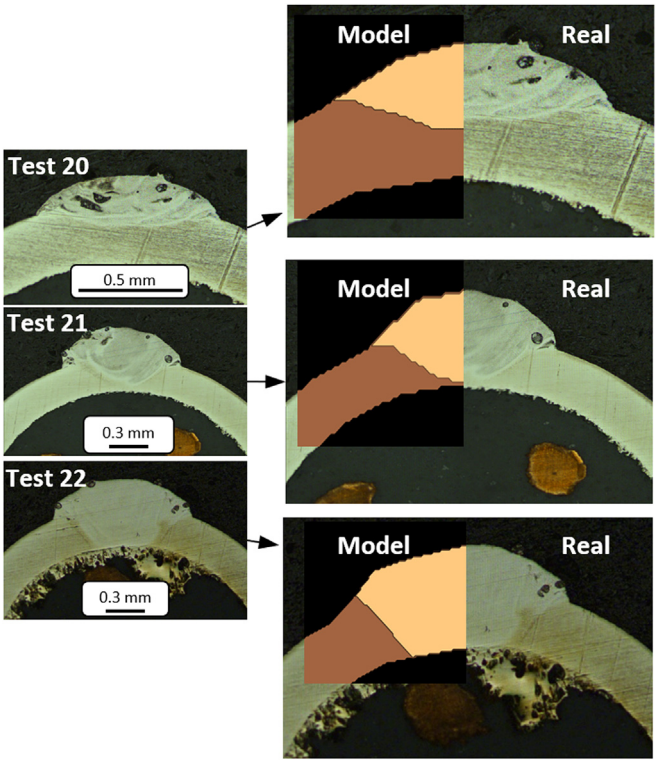

Fig. 15. Comparison between the simulated and the experimental cross section of the tests 20, 21, and 22.

Table 7
Results of the experimental tests and model for the simple clad deposition on thermocouple sheath.

Test	H (mm)			W (mm)			D (mm)			Dilution (%)
Exp.	Model	error [%]	Exp.	Model	error [%]	Exp.	Model	error [%]		
20	0.139	0.136	2.058	0.936	0.890	4.908	0.137	0.150	9.459	49.63
21	0.205	0.207	0.745	1.011	1.012	0.105	0.291	0.280	3.656	58.58
22	0.231	0.245	6.279	1.150	1.160	0.846	0.3	0.3	-	58.29

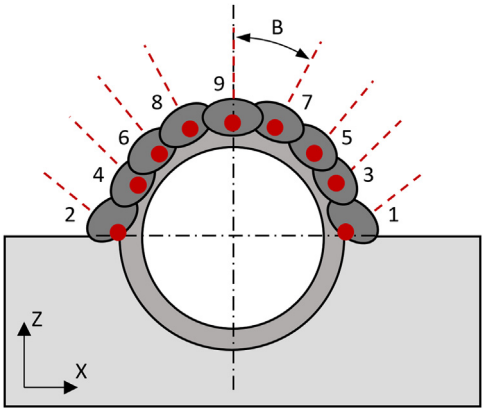

Fig. 16. Deposition strategy for Thermocouple embedding. The deposition order of the clads is numbered and the position and direction of the laser beam are represented by the red dots and dashed lines, respectively.

The numerical model does not consider the movement of the material within the melt pool. Therefore, once the wall is pierced, the model is not capable of detecting the material flow through the bottom of the wall. This is the reason why the model over predicts the thickness of the clad at the bottom. However, the model is capable of determining the laser power at which the wall is pierced and below this laser power, the model and the experimental cross sections present a higher resemblance.

7.3. Thermocouple embedding

In order to demonstrate the capabilities of the model and its applicability to real case scenarios, as a final step, a thermocouple is embedded. The model is employed for defining the process parameters (i.e. the maximum laser power) that provide good quality clads in terms of dimensions and that prevent damaging the thermocouple. Afterwards, the simulated process is experimentally executed and the proper functioning of the thermocouple is tested.

The tip of the thermocouple is 20 mm long and it has a 3 mm diameter with a 0.3 mm sheath thickness. Therefore, the same geometry and boundary conditions as in Section 7.2 are employed. The only difference is that, in this case, a total number of 9 overlapped clads need to be deposited following the scheme shown in Fig. 16. The feed rate of the machine and the powder mass flow are maintained constant during the whole process, at 450 mm·min^{-1} and 3.24 g·min^{-1}, respectively. Nevertheless, the developed model is employed for adjusting the maximum laser power in each line, and to avoid piercing the thermocouple sheath.

The first clad is deposited on the junction between the base AISI H13 and the AISI 316 sheath of the thermocouple. In this clad, the heat dissipation towards the substrate is higher than in the clads deposited on the top of the sheath. Therefore, based on the results of the model, the laser power is increased to 300 W, while the feed rate is maintained constant at 450 mm/min. On the contrary, when material is deposited directly on the casing of the thermocouple, the laser power needs to be kept below 200 W to avoid perforation.

Table 8
L-DED head positioning and process parameters for the deposition of each clad during the thermocouple embedding.

Clad	X [mm]	Z [mm]	A [°]	B [°]	Laser power [W]
1	9	5	0	45	300
2	6	5	0	-45	300
3	8.8	5.6	0	40	200
4	6.2	5.6	0	-40	200
5	8.5	6.1	0	30	200
6	6.5	6.1	0	-30	200
7	8.1	6.4	0	15	200
8	6.9	6.4	0	-15	200
9	7.5	6.5	0	0	200

Between every two consecutive clads a 30 s cooling time is imposed, which ensures a constant room temperature before every next clad deposition. Experimentally, this is validated using the same thermocouple, which is being embedded, to measure the temperature during the L-DED process. In Table 8 the process parameters and machine position for the deposition of each clad are detailed. All clads have a 20 mm length and go from y=5 mm to y=25 mm.

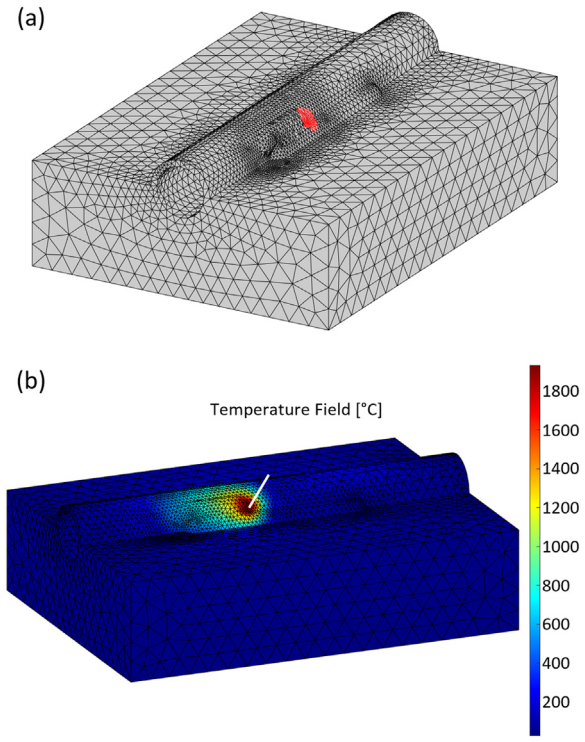

Fig. 17. (a) mesh during the deposition of clad 3, where the faces where the laser beam irradiate are highlighted in red and (b) the resulting thermal field in°C for a 200 W laser power.

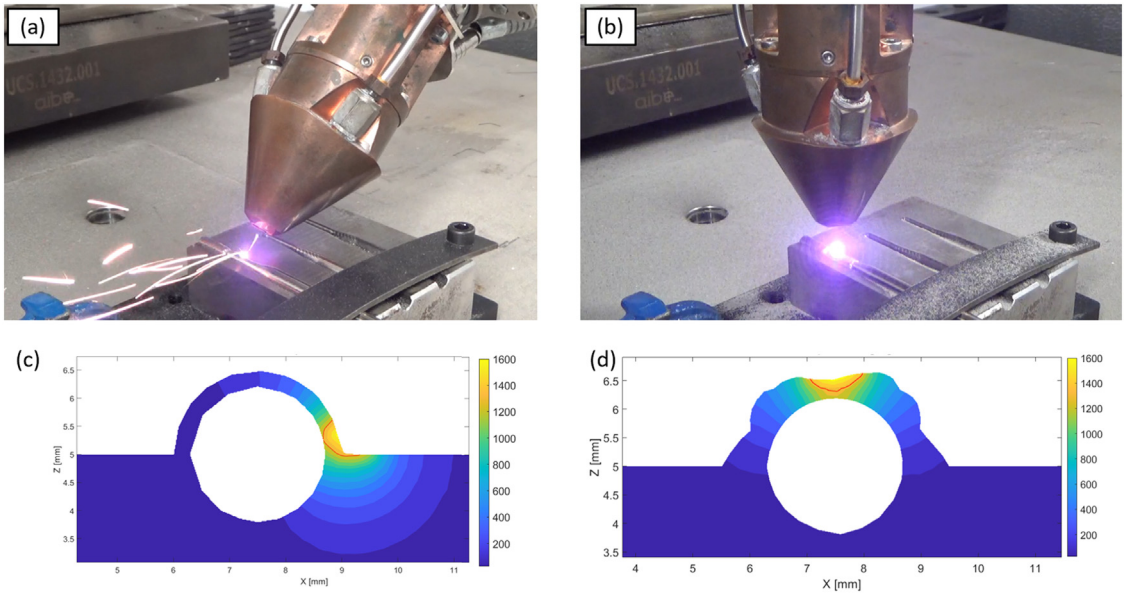

Fig. 18. (a) deposition of clad 1 and (b) clad 9 and the corresponding cross section of the simulations, (c) and (d).

In Fig. 17 the adaptive mesh and the resulting thermal field during the deposition of 3rd clad are shown. The area in red in Fig. 17(a) represents the region where the laser beam irradiates the part. The same laser beam in Fig. 17(b) is depicted by a white line. Note the refined mesh in the region where material is being deposited. This finer mesh is maintained during the whole simulation, in order to ensure the accuracy of the clad geometry and to avoid geometry degeneration in the remeshing operations of the successive time steps.

Finally, the thermocouple has been experimentally embedded using the laser power suggested by the numerical model, Table 8. In Fig. 18(a) and (b) two images of the experimental procedure are shown, corresponding to clads 1 and 9, respectively. In the deposition of the first clad, the heat distribution between the sheath and the substrate is not even. There is a risk of damaging the thermocouple if high powers are used. However, lower powers could also result in an insufficient bond between substrate and thermocouple. The lack of a metallurgical joint may inhibit a proper heat transfer from the part to the sensor. Hence, the functionality of the thermocouple could be jeopardized and the precision of the temperature measurements lowered. Consequently, the laser power should be selected as to keep a balance between the heat delivered to the sheath and the substrate. Based on the results of the numerical model, a 300 W laser power is suffice to melt the surface of the substrate, whilst avoiding piercing the sheath and damaging the thermocouple.

After the tip of the thermocouple is embedded, three more layers are deposited following the same procedure described before. As the diameter and thickness of the casing increases with every layer, the laser power can be also increased without risk of piercing the thermocouple. For the successive layers, a constant laser power was used in each layer: 300 W for the second, 400 W for the third, and 500W for the fourth and final. The resulting aspect of the embedded thermocouple is shown in Fig. 19.

Once the thermocouple is embedded, its functionality is tested by measuring the temperature rise of the sensor when heated, a video of the test is provided as supplementary material. Afterwards, the thermocouple is cross-sectioned, Fig. 19(b), and etched with Nital4 to reveal the microstructure and ensure that a sound metallurgical bond has been produced between the deposited layers of AISI H13 and the sheath of the thermocouple.

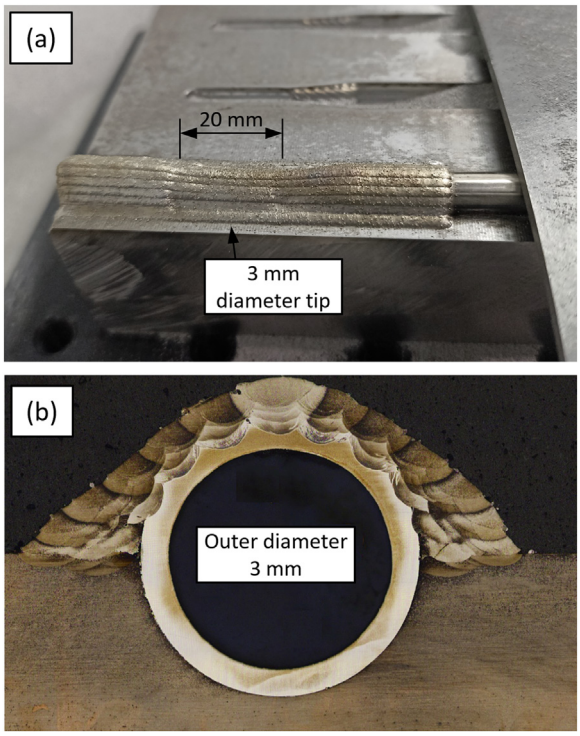

Fig. 19. a) Fully embedded thermocouple and b) a cross section.

8. Conclusions

The thermal nature of the L-DED process is a challenging issue when heat-sensitive parts are to be manufactured. To the authors' knowledge, these kinds of complex and large-scale applications have not been approached before through numerical modeling. Hence, the novelty of the present work is the development of a computationally efficient and scalable L-DED digital twin. In addition, the model is validated and its capabilities are demonstrated in a high-precision application. Namely, the developed model is employed to estimate the maximum allowable laser power for

embedding thermocouples into tooling. Hereafter are detailed the main conclusions:

- For the first time a model is used to optimize the process parameters for the direct integration of thermocouples. Besides, the validity of the L-DED process for the integration of thermocouples into tooling is demonstrated.
- The accuracy of the results and the computational cost are mesh and time step sensitive. Therefore, it is necessary to run a sensitivity analysis to ensure the reliability of the results.
- The model is capable of accurately predicting the clad geometries when depositing material onto flat surfaces. Errors below 10% are obtained in clad height, width, and dept. Nevertheless, for laser powers of 700 W and powder mass rates of 4.5 $g{\cdot}min^{-1}$, or higher values, the model losses its accuracy.
- The model provides stable clad and temperature values when depositing material onto thin-walled thermocouples. Cross section analysis proves that the model can determine the maximum allowable laser power. In the present case, 200 W is suggested for depositing material onto 3 mm diameter thermocouples without piercing their 0.3 mm thick sheath.
- The numerical modeling of the L-DED process is considered to be an appropriate tool for obtaining close to optimal process parameters, or at least, for reducing the number of trial-and-error iterations during the set-up of the L-DED process.

Nevertheless, the initial assumptions and the computational cost of the model limit the applicability of the model:

- On the one hand, the thermal field calculation and material addition model is not applicable for big size parts, because the computational cost increases with the part size. However, it is proven useful for complex small-medium sized features. The implementation of a two-scale model could solve this issue. A local model could be used for solving the heat transfer and clad generation, and a global model for geometry and thermal stress calculation. Future works are planned in this direction.
- On the other hand, the model does not consider the material movement within the melt pool. This assumption is valid for the typical powder L-DED processing window. But if higher laser diameter spots and laser powers are to be employed, the model will present a higher error. In order to consider these effects, other heat introduction mechanisms would need to be implemented in the model, rather than introducing the heat only at the surface of the irradiated part, as in the present work.
- Thirdly, assuming that the laser beam attenuation is compensated by the thermal energy gained by the powder particles before they reach the melt pool, is proven adequate. However, the increase in the powder mass rate, also causes the laser shadowing to grow and more particles to fall outside the melt pool. Thus the error of this assumption would be enhanced.

Finally, it is concluded that the PDE toolbox of the Matlab software is an appropriate tool for simulating the L-DED process. Nevertheless, the Matlab meshing tool is not as robust as desired, and it occasionally and randomly crashes. Therefore, for future works the meshing tool needs to be improved or a different meshing algorithm needs to be implemented.

Declaration of Competing Interest

The authors declare that they have no known competing financial interests or personal relationships that could have appeared to influence the work reported in this paper.

CRediT authorship contribution statement

Jon Iñaki Arrizubieta: Investigation, Methodology, Software, Writing – original draft, Writing – review & editing. **Marta Ostolaza:** Investigation, Validation, Writing – original draft, Writing – review & editing. **Maider Muro:** Investigation, Resources, Writing – original draft. **Hegoi Andonegi:** Investigation, Resources, Writing – original draft. **Aitzol Lamikiz:** Supervision, Funding acquisition, Writing – review & editing.

Data availability

Data will be made available on request.

Acknowledgements

This work was supported by the Basque Government (Eusko Jaurlaritza) through the ELKARTEK program, grant numbers KK-2022/00080 and KK-2021/00120 and the Spanish Ministry of Economy and Competitiveness under the PID2019-109220RB-I00 ALASURF project.

Supplementary materials

Supplementary material associated with this article can be found, in the online version, at doi:10.1016/j.ijheatmasstransfer.2022.123639.

References

[1] H. Alemohammad, E. Toyserkani, C.P. Paul, Fabrication of smart cutting tools with embedded optical fiber sensors using combined laser solid freeform fabrication and moulding techniques, Opt. Lasers Eng. 45 (10) (2007) 1010–1017.
[2] J. Li, B. Tao, S. Huang, Z. Yin, Cutting tools embedded with thin film thermocouples vertically to the rake face for temperature measurement, Sens. Actuators A 296 (2019) 392–399.
[3] M.S. Lee, J. Lee, H. Sung, J. Choe, H.J. Son, J. Yun, K. Kim, et al., Embedding sensors using selective laser melting for self-cognitive metal parts, Addit. Manuf. 33 (2020) 101151.
[4] S. Cooke, K. Ahmadi, S. Willerth, R. Herring, Metal additive manufacturing: Technology, metallurgy and modelling, J. Manuf. Processes 57 (2020) 978–1003.
[5] B. Dutta, Directed Energy Deposition (DED) Technology, Reference Module Mater. Sci. Mater. Eng. (2020).
[6] D. Svetlizky, M. Das, B. Zheng, A.L. Vyatskikh, S. Bose, A. Bandyopadhyay, J.M. Schoenung, E.J. Lavernia, N. Eliaz, Directed energy deposition (DED) additive manufacturing: physical characteristics, defects, challenges and applications, Mater. Today (2021) In press.
[7] X. Guan, Y.F. Zhao, Modeling of the laser powder–based directed energy deposition process for additive manufacturing: a review, Int. J. Adv. Manuf. Technol. 107 (5) (2020) 1959–1982.
[8] J. Akram, P. Chalavadi, D. Pal, B. Stucker, Understanding grain evolution in additive manufacturing through modeling, Addit. Manuf. 21 (2018) 255–268.
[9] Z. Gan, H. Liu, S. Li, X. He, G. Yu, Modeling of thermal behavior and mass transport in multi-layer laser additive manufacturing of Ni-based alloy on cast iron, Int. J. Heat Mass Transfer 111 (2017) 709–722.
[10] C.C. Tseng, C.-J. Li, Numerical investigation of interfacial dynamics for the melt pool of Ti-6Al-4V powders under a selective laser, Int. J. Heat Mass Transfer 134 (2019) 906–919.
[11] J. Gao, C. Wu, Y. Hao, X. Xu, L. Guo, Numerical simulation and experimental investigation on three-dimensional modelling of single-track geometry and temperature evolution by laser cladding, Opt. Laser Technol. 129 (2020) 106287.
[12] J. Zhao, G. Wang, X. Wang, S. Luo, L. Wang, Y. Rong, Multicomponent multiphase modeling of dissimilar laser cladding process with high-speed steel on medium carbon steel, Int. J. Heat Mass Transfer 148 (2020) 118990.
[13] C. Shen, C. Li, Y. Guo, C. Liu, X. Zhang, X. Feng, Modeling of temperature distribution and clad geometry of the molten pool during laser cladding of TiAlSi alloys, Opt. Laser Technol. 142 (2021) 107277.
[14] W. Ya, B. Pathiraj, S. Liu, 2D modelling of clad geometry and resulting thermal cycles during laser cladding, J. Mater. Process. Technol. 230 (2016) 217–232.
[15] H. Ge, H. Xu, J. Wang, J. Li, J. Yao, Investigation on composition distribution of dissimilar laser cladding process using a three-phase model, Int. J. Heat Mass Transfer 170 (2021) 120975.

[16] A. Aggarwal, A. Chouhan, S. Patel, D.K. Yadav, A. Kumar, A.R. Vinod, K.G. Prashanth, N.P. Gurao, Role of impinging powder particles on melt pool hydrodynamics, thermal behaviour and microstructure in laser-assisted DED process: A particle-scale DEM–CFD–CA approach, Int. J. Heat Mass Transfer 158 (2020) 119989.
[17] J.I. Arrizubieta, A. Lamikiz, F. Klocke, S. Martínez, K. Arntz, E. Ukar, Evaluation of the relevance of melt pool dynamics in Laser Material Deposition process modeling, Int. J. Heat Mass Transfer 115 (2017) 80–91.
[18] E. Toyserkani, A. Khajepour, S. Corbin, 3-D finite element modeling of laser cladding by powder injection: effects of laser pulse shaping on the process, Opt. Lasers Eng. 41 (6) (2004) 849–867.
[19] Y. Chew, J.H.L. Pang, G. Bi, B. Song, Thermo-mechanical model for simulating laser cladding induced residual stresses with single and multiple clad beads, J. Mater. Process. Technol. 224 (2015) 89–101.
[20] C. Guo, S. He, H. Yue, Q. Li, G. Hao, Prediction modelling and process optimization for forming multi-layer cladding structures with laser directed energy deposition, Opt. Laser Technol. 134 (2021) 106607.
[21] S. Joshi, S. Sharma, S. Mazumder, M.V. Pantawane, N.B. Dahotre, Solidification and microstructure evolution in additively manufactured H13 steel via directed energy deposition: Integrated experimental and computational approach, J. Manuf. Processes 68 (2021) 852–866.
[22] D. Wang, T. Li, B. Shi, H. Wang, Z. Xia, M. Cao, X. Zhang, An analytical model of bead morphology on the inclined substrate in coaxial laser cladding, Surf. Coat. Technol. 410 (2021) 126944.
[23] S. Sihn, L.B. Childers, C.T. Walters, M.S. Forte, A.K. Roy, J.P. Vernon, Computational and experimental study on laser heating of a Ni-based metal alloy, Int. J. Heat Mass Transfer 102 (2016) 1034–1043.
[24] W.M. Steen, J. Mazumder, Laser Material Processing, Springer-Verlag London, 2010.
[25] P. Michaleris, Modeling metal deposition in heat transfer analyses of additive manufacturing processes, Finite Elem. Anal. Des. 86 (2014) 51–60.
[26] G. Abbas, D.R.F. West, Laser surface cladding of stellite and stellite-SiC composite deposits for enhanced hardness and wear, Wear 143 (2) (1991) 353–363.